Phase transitions in ε-FeOOH at high pressure and ambient temperature

Elizabeth C. Thompson[1,*], Anne H. Davis[2], Nigel M. Brauser[2], Zhenxian Liu[3], Vitali B. Prakapenka[4], and Andrew J. Campbell[2]

[1]Department of Earth and Environmental Systems, Sewanee: The University of the South, Sewanee, Tennessee, USA,
[2]Department of the Geophysical Sciences, University of Chicago, Chicago, Illinois, USA,
[3]Department of Physics, University of Illinois, Chicago, Illinois, USA
[4]Center for Advanced Radiation Sources, University of Chicago, Chicago, Illinois, USA

*Corresponding author. Tel: +1 931-598-3321
Email: ecthomps@sewanee.edu (E. C. Thompson)

Abstract

Constraining the accommodation, distribution, and circulation of hydrogen in the Earth's interior is vital to our broader understanding of the deep Earth due to the significant influence of hydrogen on the material and rheological properties of minerals. Recently, a great deal of attention has been paid to the high-pressure polymorphs of FeOOH (space groups $P2_1nm$ and *Pnnm*). These structures potentially form a hydrogen-bearing solid solution with AlOOH and phase H ($MgSiO_4H_2$) that may transport water (OH^-) deep into the Earth's lower mantle. Additionally, the pyrite-type polymorph (space group $Pa\bar{3}$ of FeOOH), and its potential dehydration have been linked to phenomena as diverse as the introduction of hydrogen into the outer core (Nishi *et al*. 2017), the formation of Ultra Low Velocity Zones (ULVZs) (Liu *et al*. 2017), and the Great Oxidation Event (Hu *et al*. 2016). In this study, the high-pressure evolution of FeOOH was re-evaluated up to ~75 GPa using a combination of synchrotron-based X-ray diffraction (XRD), Fourier transform infrared spectroscopy (FTIR), and optical absorption spectroscopy. Based on these measurements, we report three principal findings: (1) pressure-induced changes in hydrogen bonding (proton disordering or hydrogen bond symmetrization) occur at substantially lower pressures in ε-FeOOH than previously reported and are unlikely to be linked to the high-spin to low-spin transition, (2) ε-FeOOH undergoes a 10% volume collapse coincident with an isostructural $Pnnm \rightarrow Pnnm$ structural transition at approximately 45 GPa, and (3) a pressure-induced band gap reduction is observed in FeOOH at pressures consistent with the previously reported spin transition (40 to 50 GPa).

Keywords: Phase transitions, infrared-spectroscopy, optical absorption spectroscopy, X-ray diffraction, spin transition

Introduction

The accommodation, distribution, and circulation of hydrogen in the deep Earth is key to understanding the evolution of Earth's interior due to the significant influence of hydrogen on the material and rheological properties of high-pressure phases (e.g., Sarafian *et al*. 2017; Karato 2010). Geophysical observations indicate that the Earth's upper mantle and transition zone, at least locally, host significant quantities of hydrogen (van der Meijde *et al.* 2003; Dixon *et al.* 2004, Pearson *et al.* 2014; Palot *et al*. 2016; Tschauner *et al*. 2018). Additionally, tomographic evidence supports the idea that subducting lithospheric plates pierce the transition zone, potentially ushering water into the Earth's lower mantle (van der Hilst *et al.* 1997). Yet while hydrogen in the upper mantle and transition zone is hosted primarily in nominally anhydrous phases, these phases are not stable at the high pressure and temperature conditions of the lower mantle (Hirschmann 2006). If hydrogen introduced into the lower mantle remains in the lower mantle, it is almost certainly accommodated primarily in minor hydrous phases, because the dominant lower mantle minerals (bridgmanite, ferropericlase, calcium silicate perovskite) do not have the same capacity for water storage (Bolfan-Casanova *et al*., 2002, 2003; Panero *et al*., 2015). A plausible lower mantle host is the isostructural FeOOH–AlOOH–$MgSiO_4H_2$ system.

At moderate pressures (>6 GPa) goethite (α-FeOOH, space group *Pbnm*), a widespread iron oxy-hydroxide, transforms into ε-FeOOH, an orthorhombic (space group $P2_1nm$, Z = 2) phase composed of edge-sharing FeO_6 units that are close-packed along the *c*-axis, with hydrogen atoms occupying the channels between these close-packed octahedra (Bendeliani *et al*. 1972; Pernet *et al*. 1975; Bolotina *et al.* 2008) (Figure 1a). At increased pressure, ε-FeOOH undergoes pressure-induced hydrogen bond symmetrization resulting in a second-order phase transition (space group *Pnnm*, Z = 2) (Figure 1c). However, the pressure at which this hydrogen bond symmetrization induced $P2_1nm \rightarrow Pnnm$ transition occurs remains contested (Gleason *et al*. 2008; Xu *et al*. 2013; Thompson *et al*. 2017; Ikeda *et al*. 2019). At the pressures of the Earth's lower mantle, ε-FeOOH forms a solid solution with δ-AlOOH and phase H ($MgSiH_2O_4$), creating a viable hydrogen reservoir with *P-T* stability extending from lower mantle conditions to those of the core-mantle boundary (Sano *et al*. 2008; Nishi *et al*. 2015; Xu *et al*. 2019).

Hydrogen bond symmetrization is the process by which the hydrogen in an asymmetrical O—H···O bonding unit becomes centered with respect to the two oxygens with increased

pressure, as the longer hydrogen bridge bond (H···O) compresses more rapidly than the shorter but stiffer hydroxyl bond (O—H) (Holzapfel 1972). Once the hydrogen bond is 'symmetrized', the two donor-acceptor distances are equivalent, and this shift in charge balance can lead to additional subtle structural changes (Figure 1c). In ε-FeOOH and other isostructural MOOH phases, the MO_6 octahedra shift from a slightly offset position to one centered along the two-fold axis, leading to the increase in symmetry from $P2_1nm$ to *Pnnm* (e.g., Sano-Furukawa *et al*. 2009, 2012). Alternatively, proton disorder in which both hydrogen and iron atoms are disordered over symmetric positions on the two-fold axis may also produce MOOH with *Pnnm* symmetry (Bolotina *et al*. 2008) with the resulting diffraction patterns nearly indistinguishable from symmetrized H-bond structures (e.g., Fujihara *et al*. 2002) (Figure 1b). Importantly, a recent neutron diffraction study by Sano-Furukawa *et al*. (2018), found that in δ-AlOOH, which is isostructural to ε-FeOOH, proton disordering is a precursor to hydrogen bond symmetrization. Accurately determining the pressure at which hydrogen bond symmetrization occurs is important because the phenomenon is linked to changes in compressibility (Vanpeteghem *et al.* 2003; Tsuchiya *et al*. 2005; Hushur *et al*. 2011) and due to isotopic effects may influence H/D fractionation in the deep Earth (e.g., Sano-Furukawa *et al*. 2009).

In addition to the previously described $P2_1nm \rightarrow Pnnm$ transition, ε-FeOOH reportedly undergoes a high-spin to low-spin transition, determined on the basis of X-ray diffraction (XRD) and X-ray emission spectroscopy (XES) experiments (Gleason *et al*. 2013). The XES results from Gleason *et al*. (2013) are indicative of a high-spin to low-spin transition initiated at ~40 GPa and completed at ~60 GPa. However, that study did not use a pressure-transmitting medium, which introduced significant deviatoric stress into the sample, inhibiting the detection of a sharp transition. A contemporary study by Xu *et al*. (2013), which used a pressure-transmitting medium, pinpointed this electronic transition more closely to ~45 GPa using a combination of Mössbauer spectroscopy, single-crystal diffraction, and resistivity measurements. In both studies, the authors propose causality between the hydrogen bond symmetrization and spin transition in ε-FeOOH, although Gleason *et al*. (2013) report that hydrogen bond symmetrization induces the spin transition, whereas Xu *et al*. (2013) conclude the spin transition induces hydrogen bond symmetrization. However, both studies agree that a large (~11%) volume collapse occurs coincident with the high-spin to low-spin transition, attributable to an isostructural phase transition. Significant volume reductions have been previously reported due

to high-spin to low-spin transitions without invoking hydrogen bond symmetrization, although a volume reduction of ~11% is higher than the volume reductions reported for either ferropericlase ((Mg,Fe)O) (1-3%) or ferromagnesite ((Mg,Fe)CO_3) (6-10%) (Lin *et al*. 2013), possibly due to the larger relative volume occupied by iron atoms in FeOOH compared to these phases.

In this study, we present experimental evidence of two distinct transitions in ε-FeOOH in the explored pressure range (0-70 GPa): a low-pressure (~18 GPa) second-order transition connected to hydrogen bond symmetrization and an independent first-order transition at ~45 GPa. Additionally, we report evidence of a rapid reduction in the bandgap of ε-FeOOH at pressures consistent with the previously reported spin transition.

Methods

Synthesis of ε-FeOOH for this study was performed by Akio Suzuki and is described in Suzuki (2010). The high pressures necessary for this study were achieved by compressing ε-FeOOH samples using symmetric-type diamond anvil cells (DACs) with 250 μm culet type II diamond anvils. Seventy-micron diameter sample chambers were laser ablated into stainless steel or rhenium gaskets pre-indented to 22 or 28 GPa, respectively. Powdered ε-FeOOH, kept in a desiccator prior to loading, was pressed into platelets ~3-5 μm thick and ~30 microns in diameter. Platelets of ε-FeOOH were loaded into the sample chamber, utilizing gas-loaded Ne or ~10 μm thick platelets of KBr as a pressure medium to reduce pressure gradients within the sample. Neon was loaded as a pressurized gas at the Advanced Photon Source using the COMPRES/GSECARS gas loading system (Rivers *et al*. 2008) and acted as a secondary pressure standard (Fei *et al*. 2007), with reported uncertainties based on the standard error of the (111), (200), and (220) *d*-spacings. Pressures were independently determined via the *in situ* monitoring of the R_1 luminescence line (Dewaele *et al*. 2008) of 2-3 ruby grains placed in the sample chamber, with errors reflecting the larger of either the standard deviation or 3%.

Room-temperature X-ray diffraction experiments were performed at beamline 13-ID-D (GSECARS) at the Advanced Photon Source, Argonne National Laboratory. A monochromatic (λ= 0.3344) incident X-ray beam was used, measuring 3 μm by 4 μm at full width at half maximum of the focused spot. Sample-to-detector distances and tilt were calibrated using 1-bar diffraction of LaB_6. Diffraction patterns were integrated to produce 2θ plots using DIOPTAS

(Prescher and Prakapenka 2015), positions of individual diffraction peaks were determined using PeakFit (Systat Software), and lattice parameters were calculated from the fitted *d*-spacings using the author's own Mathematica script. Individual peaks were fit to single Gaussian curves, and unresolved overlapping peaks were not used in the calculation of lattice parameters. All samples prepared for X-ray diffraction experiments were loaded using Ne as a pressure medium.

Fourier transform infrared (FTIR) spectra in this study were collected using both synchrotron and globar sources. Synchrotron experiments were performed at the 1.4.3 beamline of the Advanced Light Source at Berkeley Laboratory using a Nicolet 760 FTIR spectrometer with a custom microscope and HgCdTe detectors. Offline experiments were performed at Brookhaven National Laboratory using a Bruker Vertex 80v spectrometer and Hyperion 2000 microscope with a MCT detector. All FTIR spectra presented here reflect a spectral resolution of 4 cm^{-1}, measured wavelength ranges of 500 to 8000 cm^{-1}, and were recorded as 1024 or 512 scans. PeakFit was used for background subtraction and to obtain precise absorption peak positions using a least-squares refinement, and interference fringes in absorbance spectra were reduced mathematically in DatLab. Samples prepared for FTIR experiments used either Ne or KBr as pressure medium, and the three samples that went to the highest pressures used KBr.

Optical absorption measurements were collected at the University of Chicago. Spectra were recorded from 420 to 980 nm using a 0.3 meter focal length Princeton Instruments SP-2300i spectrograph. Transmitted light (I), generated with a tungsten filament bulb, was measured through the pressure medium (KBr) only, while incident light (I_0) was collected through the sample and pressure medium. Background measurements were collected both with the light source off and with the light source on but measured at the gasket, which is opaque, with comparable results. Interference fringes in the absorbance spectra were removed mathematically in DatLab. To account for variation in sample thickness (h), reported absorption values [$\alpha = h^{-1}\ln(I_0/I)$] have been scaled such that I_0/I is equal for all samples at 10 GPa. Samples prepared for optical absorption measurements used KBr as pressure medium.

Results and Discussion

X-ray Diffraction

High-pressure, room-temperature X-ray diffraction (XRD) measurements were used to re-evaluate the phase diagram of FeOOH up to 75 GPa, as the existing literature exhibits a paucity of volume–pressure (*V–P*) data in the mid-pressure range (20-50 GPa) (Gleason *et al*. 2008, 2013; Suzuki 2010, 2016; Ikeda *et al*. 2019). Additionally, using a gas-membrane diaphragm to remotely pressurize the DAC between diffraction measurements without manual action, data could be collected with greater pressure resolution than in previous studies. As X-ray diffraction inherently relies on electron density, the detection of hydrogen using powder XRD is virtually impossible. The $P2_1nm \rightarrow Pnnm$ transition is primarily defined by the pressure-induced symmetrization of the hydrogen bonds, but associated with hydrogen bond disordering and symmetrization are subtle changes in the structure and strain accommodation, which enable the detection of these transitions indirectly (e.g., Sano-Furukawa *et al.* 2009, 2012; Kuribayashi *et al*. 2014).

In the lower pressure interval (0.5-43 GPa) the lattice parameters of ε-FeOOH were determined using at a minimum the (110), (101), (011), (020), (210), (211), (121), (220), (002), and (301) *hkl* peaks. The resulting unit cell volumes and lattice parameters are plotted in Figures 2a and 2b and are reported in tabulated form in Table S.1. The measured lattice parameters and unit cell volumes of ε-FeOOH in this pressure interval are in excellent agreement with the results of Suzuki (2010, 2016) and Ikeda *et al*. (2019), albeit slightly lower than those reported by the Gleason *et al*. (2013). The diffraction data from Gleason *et al*. (2013) exhibit more scatter, likely due to the lack of pressure medium in that study, which likely contributed to the slight offset in measured *P–V* values.

Based on the Bragg peaks indexed in this study, the $P2_1nm$ and *Pnnm* structure cannot be distinguished from one another, as even at the lowest pressures of this study no peaks were observed that violated the additional systematic absences characteristic of the *Pnnm* symmetry ($h + l$ odd for $h0l$, $k + l$ odd for $0kl$). Additionally, based on the findings of Sano-Furukawa *et al*. (2009), who evaluated the $P2_1nm \rightarrow Pnnm$ transition in isostructural δ-AlOOH, the volume reduction associated with this second-order transition is likely unresolvable, rendering determinations of this phase boundary on this basis alone dubious. Thus, employing the approach of Sano-Furukawa *et al*. (2009, 2012), we evaluated the ratios of lattice parameters as a means of elucidating the subtle $P2_1nm \rightarrow Pnnm$ transition.

205 The evolution of the *a*/*b* and *b*/*c* lattice parameter ratios (Figure 2c) reveal a change in the
206 axial compression of ε-FeOOH with pressure, and the inflection points evident at 18±1 GPa
207 indicate a shift in the accommodation of strain in this system. Similar changes in axial
208 compression have been used previously as an indicator of second-order phase changes in similar
209 materials (e.g., Sano-Furukawa *et al*. 2009, 2012; Kuribayashi *et al*. 2014). On the basis of these
210 lattice parameter ratios, we confirm that ε-FeOOH undergoes a second-order phase transition
211 from the $P2_1nm$ to *Pnnm* structure at 18±1 GPa, in good agreement with previous predictions
212 based on density functional theory-based calculations (Thompson *et al*. 2017) and recent
213 experiments (Ikeda *et al*. 2019). As any volume reduction across this presumed phase boundary
214 is minimal (Figure 2a), the *V*–*P* data from the entire pressure interval (0 to 45 GPa) was fit to a
215 third-order Birch-Murnaghan equation of state (EoS) (Birch 1978):

216 $$P(V,T) = 3K_0 f_E \left[(1+2f_E)^{\frac{5}{2}}\left(1+\frac{3}{2}[K_0'-4]f_E\right)\right]$$

217 which relates pressure (P), volume (V), ambient pressure bulk modulus (K_0), and its pressure
218 derivative (K_0') in terms of finite Eulerian strain (f_E):

219 $$f_E = \frac{1}{2}\left[\left(\frac{V_0}{V}\right)^{\frac{2}{3}} - 1\right]$$

220 which is a measure of the volume compression of a solid relative to its initial volume (V_0).
221 Residuals from this fit are shown in Figure S1.

222 To obtain EoS parameters with the most comprehensive data set available, the *V*–*P* data
223 from this study and Suzuki (2010, 2016) were combined, and the resultant equation of state
224 parameters are presented alongside parameters fit to the data from only this study. In addition to
225 fitting *V*–*P* data from the entire 0-45 GPa pressure range, we also report EoS parameters derived
226 from fitting the *V*–*P* data of the $P2_1nm$ and *Pnnm* structures separately. The resultant EoS
227 parameters, as well as previously published results, are reported in Table 1. We find that EoS
228 parameters derived from fitting the combined data set across the entire pressure range (0-45 GPa)
229 are in reasonable agreement with those reported by Gleason *et al*. (2008) and Suzuki (2010,
230 2016). However, fitting *V*–*P* data for the $P2_1nm$ and *Pnnm* structures independently (using a
231 fixed K_0' value of 4 because fewer fitted parameters are justified over the limited pressure
232 ranges), reveals that the P*nnm* structure has a bulk modulus ~20% higher than that of the $P2_1nm$
233 ε-FeOOH, in good agreement with the ~19% predicted from DFT calculations (Thompson *et al*.

2017). These findings are also in good agreement with a prior study by Xu *et al.* (2013) that identified a reduction in the compressibility of FeOOH at ~16 GPa but did not connect this change in material properties to the onset of pressure-induced hydrogen bond symmetrization or proton disordering. Similar increases in bulk modulus have been reported for other hydrous phases due to the onset of pressure-induced hydrogen bond symmetrization or proton disordering (Vanpeteghem *et al.* 2003; Tsuchiya *et al*. 2005; Hushur *et al*. 2011).

Additionally, XRD data from this study revealed a second, independent structural transition in ε-FeOOH at ~45 GPa. The transition occurs over a small (<3 GPa) pressure interval and is evident in the appearance of multiple new Braggs peaks and a simultaneous reduction in the intensity, and eventual disappearance, of the Braggs peaks of the high-spin *Pnnm* structure (Figure 3). This high-pressure (> 45 GPa) structure of FeOOH is stable at ambient temperatures and pressures exceeding 70 GPa. While an earlier study identified a potential unit cell volume reduction in this pressure range (Gleason *et al*. 2013), the improved pressure resolution of the current study clarifies the pressure at which this transition occurs. The sharpness of this phase boundary and the significant volume reduction contrast with the gradual, displacive second-order transition produced by the gradual change in charge density due to hydrogen bond symmetrization. Conversely, the structural transition observed at ~45 GPa is within the pressure range in which the high-spin to low-spin transition has been observed (Gleason *et al*. 2013), and the contraction of the Fe^{3+} ionic radius across the high-spin to low-spin transition has been reported to produce significant volume reductions in other iron-bearing minerals (e.g., Lin *et al*. 2013). Although the <3 GPa interval in which the first-order transition is observed in this study is significantly narrower than the 20 GPa pressure interval across which the high-spin to low-spin transition was reported (Gleason *et al.* 2013), this discrepancy may be due to the lack of a pressure medium in the earlier study, an omission that can produce pressure gradients that could lead to significantly broader spin transitions.

High-pressure (>45 GPa) X-ray diffraction data from this study were indexed to a *Pnnm* (Z=2) unit cell, using at a minimum the (110), (200), (011), (121), (310), (301), and (112) *d*-spacings. The resultant lattice parameters and unit cell volumes are consistent with a volume reduction of 10% without a loss of symmetry, in reasonable agreement with the isostructural, 11% volume collapse proposed by Gleason *et al*. (2013) (Figure 2a). However, a recent *ab initio* study has predicted an intermediate *Pbca* (Z=8) structure is stable between the *Pnnm* and the

pyrite ($Pa\bar{3}$) phases of AlOOH (Verma *et al*. 2018). The high-pressure (>45 GPa) XRD data from this study was indexed to the proposed *Pbca* structure, but the reduction in volume across this potential *Pnnm* → *Pbca* transition appears implausibly large (26%) and resulted in a reduced quality of fit. An attempt was made to index the high-pressure Bragg peaks to the α-PbO_2 structure (*Pbcn*), a structure adopted by $CaCl_2$ -type (*Pnnm*) oxides at high pressures, but this failed to produce a reasonable fit to the data. Additionally, we can definitively state that this is not the appearance of the high-pressure pyrite structure of FeOOH, to which ε-FeOOH is expected to transition at comparable pressures and elevated temperatures (Nishi *et al*. 2017; Hu *et al*. 2016). Therefore, we interpret the first-order transition at 45±2 GPa as an isostructural volume collapse (i.e., *Pnnm* → *Pnnm)*, accompanied by an increase in the *a*/*b* ratio in the higher-pressure structure (Figure 2d). The change in the *a*/*b* ratio may be due to a relaxation of the distortion of the FeO_6 units, in agreement with Xu *et al*. (2013) and linked to the previously reported high-spin to low-spin transition (Gleason *et al.* 2013; Xu *et al.* 2013). In the future, single crystal X-ray diffraction structure refinements might help elucidate the nature of this structural transition (displacive versus reconstructive) and refine the symmetry of the high pressure, low-spin structure.

Infrared and Visible Absorption Spectroscopy

Room temperature infrared absorption spectra of ε-FeOOH were collected at ambient pressure and at regularly increasing pressure intervals of ~2 GPa up to ~50 GPa. Qualitatively, the ambient pressure ε-FeOOH spectrum bears similarity to that of $P2_1nm$ β-CrOOH, with which ε-FeOOH is isosymmetric (Jahn *et al*. 2012) (Figure 4). At ambient pressure, the O-H stretching region presents as a broadband feature (2600-3100 cm^{-1}), consistent with previously reported spectra of low-pressure polymorphs of FeOOH (e.g., Williams and Garnero 1996; Kagi *et al*. 2008), and with increased pressure, the broadband O-H stretching region further broadens and shifts to lower wavenumbers. Unfortunately, the increased breadth of the O-H stretching feature and its increased proximity to the diamond absorption region prevents tracking the pressure dependence of this feature above ~17 GPa. Although the O-H stretching band could only be monitored over a limited pressure range, its negative frequency shift pressure dependence was clearly observable at low pressures (Figure S3). A linear fit of the pressure-frequency data of the

O-H stretching band results in an approximate pressure dependence of −14 $cm^{-1}GPa^{-1}$, demonstrative of a softening behavior consistent with eventual hydrogen bond symmetrization. However, it isn't feasible to predict the pressure of eventual hydrogen bond symmetrization, as the relationship between the 1-bar stretching frequency and O-H pressure dependence is poorly understood in ε-FeOOH and similarly structured phases, and the pressure range of available ε-FeOOH O-H stretching frequency data is limited.

The ambient pressure infrared spectrum of ε-FeOOH also contains three distinct absorption bands at 965, 1145, 1175 cm^{-1} that were identified as O-H bending vibrations based on comparison to similar structures (Williams and Garnero, 1996; Mashino *et al*. 2016; Pinney and Morgan 2013). Spectra at successive pressure steps were evaluated to determine the frequency shifts in the O-H bending as a function of pressure (Figure 5). As with the OH-stretching region, these features broaden with increased pressure, and the two higher frequency bands become indistinguishable above 17.5±1 GPa. The lowest-frequency bending band remains distinct to higher pressures, but the pressure dependence of this band changes dramatically above 17.5±1 GPa. The sudden change in the pressure dependence of this band suggests a reorientation of the O-H bonds, suggestive of the onset of pressure-induced hydrogen bond symmetrization or proton disordering. A similar shift in the pressure dependence of the OH-absorption bands in isostructural δ-AlOOH was observed by Kagi *et al*. (2010) at approximately 10 GPa, consistent with the onset of proton disordering in that phase (Sano-Furukawa *et al*. 2018).

During the course of these IR measurements, a reduction in the transmitted IR signal was observed in ε-FeOOH samples compressed above ~40 GPa (Figure S4). In addition to the changes in IR transmission properties, changes in the optical properties of FeOOH were observed upon compression. The samples were translucent orange at ambient and low pressures, but reddened with increased pressure and became opaque to transmitted visible light at 45 GPa, slightly preceding the loss of IR transmission (Figure S4). To quantify these observations, visible to near-infrared absorption measurements of ε-FeOOH were collected up to pressures exceeding 70 GPa, to track the pressure dependence of the absorption edge. Representative high-pressure optical absorption spectra of ε-FeOOH are shown in Figure 6a and indicate a systematic pressure-induced increase in absorption concordant with qualitative observations. Normalized data for five samples are plotted in Figure 6b, in which there are two key features. First, each sample underwent a transient minimum in optical transmission between 15-20 GPa before

gradually recovering to previous values over the subsequent ~5 GPa. Second, all five samples became opaque in the light range probed (1.45 eV to 2.05 eV) above 50 GPa (Figure 6b), above which the ratio of transmitted light (I) to incident light (I_0) that can propagate through the sample decreases to zero. These vis/NIR absorption findings suggest a significant reduction in the bandgap in this pressure interval.

Implications

Close evaluation of the high-pressure behavior of ε-FeOOH at ambient temperature indicates two sequential, structural phase transitions in the 0-75 GPa pressure range. A second-order transition at 18±1 GPa was determined on the basis of three observations: (1) a change in axial compressibility evident in the lattice parameter ratios measured using powder XRD, (2) a change in the OH-bending modes observed with FTIR spectroscopy, and (3) a transient decrease in optical absorption. In accordance with the previous work of Sano-Furukawa *et al.* (2009, 2012, 2018) that evaluated isostructural MOOH phases, this 18±1 GPa transition is the $P2_1nm \rightarrow Pnnm$ transition produced by either pressure-induced hydrogen bond symmetrization or proton disordering, with future neutron diffraction work needed to differentiate between these mechanisms. Furthermore, this transition is observed to lead to a ~20% increase in bulk modulus and could be linked to the increase in compressional velocity (V_P) reported by Ikeda *et al.* (2019).

At 45±2 GPa, *Pnnm* ε-FeOOH undergoes a first-order structural phase transition, identifiable due to the appearance of new Bragg peaks coincident with the disappearance of the high-spin *Pnnm* peaks. This high-pressure structure of FeOOH can also be indexed to *Pnnm* with a ~10% volume reduction, in good agreement with previous studies (Gleason *et al*. 2013; Xu *et al.* 2013). Therefore, we propose that the first-order transition at 45±2 GPa is a nearly isostructural volume collapse (i.e., *Pnnm* → *Pnnm)*, accompanied by a small (~1%) increase in the a/b ratio in the higher-pressure structure (Figure 2d). As such, low-spin *Pnnm* FeOOH is stable across a wide pressure range (more than 30 GPa). However, the phase diagram of FeOOH at high pressures and moderate temperatures should be assessed to determine the relevance of low-spin *Pnnm* FeOOH to the Earth's interior, as the formation of the pyrite ($Pa\bar{3}$) structure is reported at comparable pressures and high temperatures (Nishi *et al*. 2017; Hu *et al*. 2016). In the

358 future, single crystal X-ray diffraction structure refinements may be beneficial in verifying the
359 symmetry of this higher pressure, low-spin structure.

360 In addition to the first-order structural transition identified in FeOOH at ~45 GPa, a color
361 change (translucent orange to black) was observed at high pressure, and the optical opacity of
362 *Pnnm* ε-FeOOH was quantified using visible/NIR transmission and infrared absorption. Visible
363 to near-infrared absorption measurements of ε-FeOOH also identified a systematic pressure-
364 induced increase in absorption consistent with band gap reduction in the high-spin *Pnnm* phase,
365 although complete band gap collapse (i.e., metallization) of this phase cannot be established on
366 the basis of these experiments alone. FeOOH becomes opaque in the 1.45-2.05 eV range and
367 also in the mid-IR at 45 GPa, indicating a change in optical properties along with the high-spin to
368 low-spin transition in this material, as both phenomena are tied to changes in the d orbitals of the
369 iron atoms. In fact, a similar increase in optical opacity has been previously linked to the high-
370 spin to low-spin transition in siderite (Lobanov *et al.* 2015) and ferropericlase (Keppler *et al*.
371 2007). The apparent width of this transition, when compared to the sharpness of the structural
372 transition observed using diffraction, may be attributable to the difference in the hydrostaticity of
373 the pressure medium (KBr and Ne, respectively).

374 These results demonstrate that bandgap reduction, the previously observed high-spin to
375 low-spin spin transition (Gleason *et al.* 2013; Xu *et al.* 2013), and the first-order phase transition
376 in ε-FeOOH all occur at a pressure (45±2 GPa) greatly exceeding the $P2_1nm \rightarrow Pnnm$ symmetry
377 transition associated with a change in hydrogen bonding (18±1 GPa). Therefore, hydrogen-bond
378 symmetrization is not the driver of spin transition in ε-FeOOH or vice versa. Rather, FeOOH
379 undergoes a second-order $P2_1nm \rightarrow Pnnm$ symmetry change caused by a shift in hydrogen
380 bonding at 18 GPa, and a subsequent, unrelated first-order transition at 45 GPa that involves a
381 significant volume change, spin transition, and optical opacity. Furthermore, although
382 endmember ε-FeOOH is expected to transition to the pyrite ($Pa\bar{3}$) structure at the concurrent
383 pressures and high temperatures of the Earth's mantle (Nishi *et al*. 2017; Hu *et al*. 2016),
384 aluminum substitution is expected to increase the thermodynamic stability of (Fe,Al)OOH such
385 that the low-spin *Pnnm* structure may be stable at the conditions of the deep Earth (e.g., Nishi *et*
386 *al*. 2015; Xu *et al*. 2019). We anticipate that the high-spin to low-spin spin transition and
387 associated volume collapse in intermediate compositions in the FeOOH–AlOOH–$MgSiH_2O_4$
388 system are likely to occur at lower pressures than in the Fe-endmember, as has been observed in

ferropericlase (Fei *et al*. 2007). Additional experiments are needed to assess the influence of cation substitution on the phase boundaries of the FeOOH−AlOOH−$MgSiO_4H_2$ system, as this may play a pivotal role in the transport of water (OH^-) deep into the Earth's lower mantle (Ohira *et al*. 2014, Xu *et al*. 2019) and may contribute to geophysical heterogeneities observed in the deep Earth (Thompson *et al*. 2017; Ohira *et al*. 2019).

Acknowledgments

The authors declare no real or perceived financial conflicts of interest related to this work. Supporting information can be found in the supplemental documents. The authors thank M.M. Reagan for providing sample material, which was originally synthesized by A. Suzuki. This work was supported by a National Science Foundation (NSF) EAR Postdoctoral Fellowship under grant EAR-1725673 for E.C.T. and NSF Grant EAR-1651017 for A.J.C. The FTIR facilities at the National Synchrotron Light Source is supported by Consortium for Materials Properties Research in Earth Sciences (COMPRES) under NSF Cooperative Agreement EAR-1143050 and by the U.S. Department of Energy, Office of Science, Office of Basic Energy Sciences, under Contract DE-AC02-98CH10886. Use of the COMPRES-GSECARS gas loading system was supported by COMPRES under NSF Cooperative Agreement EAR-1606856 and by GSECARS through NSF grant EAR-1634415 and DOE grant DE-FG02-94ER14466. This research used resources of the Advanced Photon Source, a U.S. Department of Energy (DOE) Office of Science User Facility operated for the DOE Office of Science by Argonne National Laboratory under Contract No. DE-AC02-06CH11357. We also thank three anonymous reviewers whose comments helped improve this manuscript.

References

Bendeliani, N. A., Baneyeva, M. I., and Poryvkin, D. S. (1972). Synthesis of a new modification of FeO(OH) stable at high pressures. Geokhimiya, 7:871-873. AN: 020182293

Birch, F. (1978). Finite strain isotherm and velocities for single crystal and polycrystalline NaCl at high-pressures and 300 K. Journal of Geophysical Research, 83:1257-1268. doi: 10.1029/JB083iB03p01257

Blanchard, M., Balan, E., Giura, P., Béneut, K., Haohao, Y., Guillaume, M., Pinilla, C., Lazzeri, M. and Floris, A. (2014). Infrared spectroscopic properties of goethite: Anharmonic broadening, long-range electrostatic effects and Al substitution. Phys. Chem. Miner. 41:289-302. doi: 10.1007/s00269-013-0648-7

Bolfan-Casanova, N., Mackwell, S. J., Keppler, H., McCammon, C. A. and Rubie, D. C. (2002), Pressure dependence of H solubility in magnesiowüstite up to 25 GPa: Implications for the storage of water in the Earth's lower mantle, Geophysical Research Letters, 29(10) :891-894, doi:10.1029/2001GL014457

Bolfan-Casanova, N., H. Keppler, and D. C. Rubie (2003), Water partitioning at 660 km depth and evidence for very low water solubility in magnesium silicate perovskite, Geophysical Research Letters, 30(17), 1905, doi:10.1029/2003GL017182

Bolotina, N., Molchanov, V., Dyuzheva, T., Lityagina, L., and Bendeliani, N. (2008). Single-crystal structures of high-pressure phases FeOOH, FeOOD, and GaOOH. Chrystallography Reports, 53:960. doi: 10.1134/S1063774508060084

Dewaele, A., Torrent, M., Loubeyre, P., and Mezouar M. (2008). Compression curves of transition metals in the Mbar range: Experiments and projector augmented-wave calculations. Physical Review B, 78:104102. doi: 10.1103/PhysRevB.78.104102

Dixon, J.E., Dixon, T.H., Bell, D.R., and Malservisi, R. (2004). Lateral variation in upper mantle viscosity: Role of water. Earth and Planetary Science Letters, 222:451-467. doi: 10.1016/j.epsl.2004.03.022

Fei, Y., Ricolleau, A., Frank, M., Mibe, K., Shen, G., and Prakapenka, V. (2007). Toward an internally consistent pressure scale. Proceedings of the National Academy of Sciences, 104(22):9182-9186. doi: 10.1073/pnas.0609013104

Fujihara, T., Ichikawa, M., Gustafsson, T., Olovsson, I. and Tsuchida, T. (2002). Powder-neutron diffraction studies of geometric isotope and hydrogen-bonding effects in β-CrOOH. Journal of Physics and Chemistry of Solids, 63:309-315. doi: 10.1016/S0022-3697(01)00147-0

Gleason, A., Jeanloz, R., and Kunz, M. (2008). Pressure-temperature stability studies of FeOOH using X-ray diffraction. American Mineralogist, 93:11-12. doi: 10.2138/am.2008.2942

Gleason, A., Quiroga, C., Suzuki, A., Pentcheva, R., and Mao, W. (2013). Symmetrization driven spin transition in ε-FeOOH at high pressure. Earth and Planetary Science Letters, 379:49–55. doi: 10.1016/j.epsl.2013.08.012

Hirschmann, M. (2006). Water, Melting, and the Deep Earth H_2O Cycle. Annual Review of Earth and Planetary Sciences, 34:629-653. doi: 10.1146/annurev.earth.34.031405.125211

Holzapfel, W.B. (1972). On the symmetry of the hydrogen bonds in ice VII. The Journal of Chemical Physics, 56:712. doi: 10.1063/1.1677221

Hu, Q., Kim, D., Liu, J., Meng, Y., and Mao, H.-K. (2016). FeO_2 and FeOOH under deep lower-mantle conditions and Earth's oxygen-hydrogen cycles. Nature, 534:241-245. doi: 10.1038/nature18018

Hushur, A., Manghnani, M.H., Smyth, J.R., Williams, Q., Hellebrand, E., Lonappan, D., Ye, Y., Dera, P., and Frost, D.J. (2011). Hydrogen bond symmetrization and equation of state of phase D. Journal of Geophysical Research, 116:B06203. doi: 10.1029/2010JB008087

Ikeda, O., Sakamaki, T., Ohashi, T., Goto, M., Higo, Y., and Suzuki, A. (2019). Sound velocity mesurements of ε-FeOOH up to 24 GPa. Journal of Mineralogical and Petrological Sciences. doi: 10.2465/jmps.181115b

Jahn, S., Wunder, B., Kock-Müller, M., Tarrieu, L., Pöhle, M., Watenphul, A., and Taran, M. (2012). Pressure-induced hydrogen bond symmetrization in guyanaite, β-CrOOH: evidence from spectroscopy and *ab initio* simulations. European Journal of Mineralogy, 24:839-850. doi: 10.1127/0935-1221/2012/0024-2228

Kagi, H., Ushijima, D., Iizuka, R., Nakano, S., and Nagai, T. (2008). Micro-pellet method for infrared absorption spectroscopy using a diamond anvil cell under a quasi-hydrostatic condition. High Pressure Research, 28(3):299-306. doi: 10.1080/08957950802346868

Kagi, H., Ushijima, D., Sano-Furukawa, A., Komatsu, K., Iizukam R., Nagai, T., and Nakano, S. (2010). Infrared absorption spectra of δ-AlOOH and its deuteride at high pressure and implication to pressure response of the hydrogen bonds. Journal of Physics: Conference Series, 215: 012052. doi: 10.1088/1742-6596/215/1/012052

Karato, S. (2010). Rheology of the deep upper mantle and its implications for the preservation of the continental roots: A review. Tectonophysics, 481:82-98. doi: 10.1016/j.tecto.2009.04.011

480 Keppler, H., Kantor, I., and Dubrovisnky, L. (2007). Optical absorption spectra of ferropericlase
481 to 84 GPa. American Mineralogist, 92:433-436. doi: 10.2138/am.2007.2454
482 Kuribayashi, T., Sano-Furukawa, A., and Nagase, T. (2014). Observation of pressure-induced
483 phase transition of δ-AlOOH by using single crystal synchrotron X-ray diffraction
484 method. Physics and Chemistry of Minerals, 41:303-312. doi: 10.1007/s00269-013-0649-
485 6
486 Lin, J.-F., Speaziale, S., Mao, Z., and Marquardt, R. (2013). Effects of the electronic spin
487 transitions of iron in lower mantle minerals: Implications for deep mantle geophysics and
488 geochemistry. Reviews of Geophysics, 51(2):244-275. doi: 10.1002/rog.20010
489 Lobanov, S. S., Goncharov, A. F., and Litasov, K. D. (2015). Optical properties of siderite
490 (FeCO3) across the spin transition: Crossover to iron-rich carbonates in the lower mantle.
491 American Mineralogist, 100(5-6), 1059-1064.
492 Mashino, I., Murakami, M., and Ohtani, E. (2016). Sound velocities of δ-AlOOH up to core-
493 mantle boundary pressures with implications for the seismic anomalies in the deep
494 mantle. Journal of Geophysical Research: Solid Earth, 121:595-609. doi:
495 10.1002/2015JB012477
496 Momma, K. and Izumi, F. (2008). VESTA: a three-dimensional visualization system for
497 electronic and structural analysis. Journal of Applied Crystallography, 41:653-658. doi:
498 10.1107/S0021889808012016
499 Nishi, M., Irifune, T., Greaux, S., Tange, Y., and Higo, Y. (2015). Phase transitions of serpentine
500 in the lower mantle. Physics of the Earth and Planetary Interiors, 245:52-58. doi:
501 10.1016/j.pepi.2015.05.007
502 Nishi, M., Kuwayama, Y., Tsuchiya, J., and Tsuchiya, T. (2017). The pyrite-type high- pressure
503 form of FeOOH. Nature, 547:205-208. doi: 10.1038/nature22823
504 Ohira, I., Ohtani, E., Sakai, T., Miyahara, M., Hirao, N., Ohishi, Y., and Nishijima, M. (2014).
505 Stability of a hydrous δ-AlOOH−$MgSiO_2(OH)_2$, and a mechanism for water transport
506 into the base of lower mantle. Earth and Planetary Science Letters, 401:12-17. doi:
507 10.1016/j.epsl.2014.05.059
508 Ohira, I., Jackson, J.M., Solomatova, N.V., Sturhahn, W., Finkelsteinm G.J., Kamada, S.,
509 Kawazoe, T., Maeda, F., Hirao, N., Nakano, S., Toellner, T.S., Suzuki, A. and Ohtani, E.

(2019). Compressional behavior and spin state of δ-(Al,Fe)OOH at high pressure. American Mineralogist, 104(9):1273-1284. doi: 10.2138/am-2019-6913

Panero, W.R., Pigott, J.S., Reaman, D.M., Kabbes, J.E., and Liu, Z. (2015). Dry (Mg,Fe)SiO_3 perovskite in the Earth's lower mantle. Journal of Geophysical Research: Solid Earth, 100(2):894-908. doi: https://doi.org/10.1002/2014JB011397

Palot, M., Jacobsen, S.D., Townsend, J.P., Nestola, F., Marquardt, K., Miyajim, N., Harris, J.W., Stachel, T., McCammon, C.A., Pearson, D.G. (2016). Evidence for H_2O-bearing fluids in the lower mantle from diamond inclusion. Lithos, 265:237-243. doi: 10.1016/j.lithos.2016.06.023

Pearson, D.G., Brenker, F.E., Nestola, F., McNeill, J., Nasdala, L., Hutchison, M.T., Matveev, S., Mather, K., Silversmit, G., Schmitz, S., Vekemans, B. and Vincze, L. (1975). Hydrous mantle transition zone indicated by ringwoodite included within diamond. Nature, 507:221-224. doi: 10.1038/nature13080

Pernet, M., Joubert, J., and Berthet-Colominas, C. (1975). Etude par diffraction neutronique de la forme haute pression de FeOOH. Solid State Communications, 17:1505–1510. doi: 0.1016/0038-1098(75)90983-7

Pinney, N. and Morgan, D. (2013). Ab initio study of structurally bound water at cation vacancy sites in Fe- and Al-oxyhydroxide materials. Geochimica et Cosmochimica Acta, 114:94-111. doi: 10.1016/j.gca.2013.03.032

Prescher, C. and Prakapenka, V. (2015). DIOPTAS: a program for reduction of two-dimensional X-ray diffraction data and data exploration. High Pressure Research, 35(3):223-230. doi: 10.1080/08957959.2015.1059835

Rivers, M., Prakapenka, V., Kubo, A., Pullins, C., Holl, C., and Jacobsen, S. (2008). The COMPRES/GSECARS gas-loading system for diamond anvil cells at the Advanced Photon Source. High Pressure Research, 28:273–292. doi: 10.1080/08957950802333593

Sano, A., Ohtani, E., Kondo, T., Hirao, N., Sakai, T., Sata, N., Ohishi, Y., and Kikegawa, T. (2008). Aluminous hydrous mineral δ-AlOOH as a carrier of hydrogen into the core-mantle boundary. Geophysical Research Letters, 35:L03303. doi: 10.1029/2007GL031718

Sano-Furukawa, A., Kagi, H., Nagai, T., Nakano, S., Fukura, S., Ushijim, D., Iizuka, E., and Yagi, T. (2009). Change in compressibility of δ-AlOOD and δ-AlOOH at high pressure:

A study of isotope effect and hydrogen-bond symmetrization. American Mineralogist, 94:1255–1261. doi: 10.2138/am.2009.3109

Sano-Furukawa, A., Yagi, T., Okada, T., Gotou, H., and Kikegawa, T. (2012). Compression behaviors of distorted rutile-type hydrous phases, MOOH (M=Ga, In, Cr) and CrOOD. Physics and Chemistry of Minerals, 39:375–383. doi: 10.1007/s00269-012-0487-y

Sano-Furukawa, A., Hattori, T., Komatsu, K., Kagi, H., Nagai, T., Molaison, J.J., dos Santos, A.M. and Tulk, C.A. (2018). Direct observation of symmetrization of hydrogen bond in δ-AlOOH under mantle conditions using neutron diffraction. Scientific Reports, 8:15520. doi: 10.1038/s41598-018-33598-2

Sarafian, E., Gaetani, G.A., Hauri, E.H., and Sarafian, A.R. (2017). Experimental constraints on the damp peridotite solidus and oceanic mantle potential temperature. Science, 355(6328):942–945. doi: 10.1126/science.aaj2165

Syassen, K. (2012) Computer Code DATLAB, Max Planck Institute, Stuttgart, Germany.

Sørensen, H.O., Schmidt, S., Wright, J.P., Vaughan, G.B.M., Techert, S., Garman, E.F., Oddershede, J., Davaasambu, J., Paithankar, K.S., Gundlach, C., and Poulsen, H.F. (2012). Multigrain crystallography. Zeitschrift für Kristallographie, 227:63-78. doi: 10.1524/zkri.2012.1438

Suzuki, A. (2010). High-pressure X-ray diffraction study of ε-FeOOH. Physics and Chemistry of Minerals, 37:153–157. doi: 10.1007/s00269-009-0319-x

Suzuki, A. (2016). Pressure-volume-temperature equation of state of ε-FeOOH to 11 GPa and 700 K. Journal of Mineralogical and Petrological Sciences, 111:420–424. doi: 10.2465/jmps.160719c

Thompson, E., Campbell, A., and Tsuchiya, J. (2017). Elasticity of ε-FeOOH: Seismic implications for Earth's lower mantle. Journal of Geophysical Research Solid Earth, 122(7):5038–5047. doi: 10.2138/am-2016-5465

Tschauner, O., Haung, S., Greenberg, E., Prakapenka, V.B., Ma, C., Rossman, G.R., Shen, A.H., Zhang, D., Newville, M., Lanzirotti, A., and Tait, K. (2018). Ice-VII inclusions in diamonds: Evidence for aqueous fluid in Earth's deep mantle. Science, 359:1136-1139. doi: 10.1126/science.aao3030

570 Tsuchiya, J., Tsuchiya, T., and Tsuneyuki, S. (2005). First-principles study of hydrogen bond
571 symmetrization of phase D under high pressure. American Mineralogist, 90:44-49. doi:
572 10.2138/am.2005.1628
573 van der Hilst, R. D., Widiyantoro, S., and Engdahl, E. R. (1997). Evidence for deep mantle
574 circulation from global tomography. Nature, 386:578-584. doi: 10.1038/386578a0
575 van der Meijde, M., Marone, F., Giardini, D., and van der Lee, S. (2003). Seismic evidence for
576 water deep in the Earth's upper mantle. Science, 300:1556-1558. doi:
577 10.1126/science.1083636
578 Vanpeteghem, C.B., Ohtani, E., Kondo, T., Takemura, K. and Kikegawa, T. (2003).
579 Compressibility of phase Egg AlSiO3OH: Equation of state and role of water at high
580 pressure. American Mineralogist, 88:1408-1411. doi: 10.2138/am-2003-1002
581 Verma, A.K., Modak, P., and Stixrude, L. (2018). New high pressure phases in MOOH (M = Al,
582 Ga, In). American Mineralogist, 103:1906-1917. doi: 10.2138/am-2018-6634
583 Williams, Q. and Garnero, E. (1996). Seismic evidence for partial melt at the base of Earth's
584 mantle. Science, 273:1528–1530. doi: 10.1126/science.273.5281.1528
585 Xu, W., Greenberg, E., Rozenberg, G., Pasternak, M., Bykova, E., Boffa-Ballaran, T.,
586 Dubrovinsky, L., Prakapenka, V., Hanfland, M., Vekilova, O., Simak, S., and Abrikosov,
587 I. (2013). Pressure-induced hydrogen bond symmetrization in iron oxyhydroxide.
588 Physical Review Letters, 111(17):175501. doi: 10.1103/PhysRevLett.111.175501
589 Xu, C., Nishi, M., and Inoue, T. (2019). Solubility behavior of δ-AlOOH and ε-FeOOH at high
590 pressures. American Mineralogist, 104: 1416–1420. doi: 10.2138/am-2019-7064
591
592
593

Tables

Table 1. Birch-Murnaghan equation of state (EoS) parameters of ε-FeOOH, including ambient-pressure unit volume (V_0), bulk modulus (K_0), and the pressure derivative of the bulk modulus (K_0'). Also included is the pressure range of the included room-temperature XRD data and the number of *V–P* data points included in each EoS fitting. The first and second lines are parameters obtained from fitting the same data to second- and third-order BM EOSs, respectively. Values in parentheses are uncertainties on the last digit. Residuals from the fit to a third-order Birch-Murnaghan equation of state are shown in Figure S1.

	Pressures (GPa)	# Data points	V_0 (Å^3)	K_0 (GPa)	K_0'
This study	0 to 45	59	65.87(3)	152(4)	4.9(2)
This study	0 to 45	59	65.57(6)	170(1)	4 (fixed)
This study, Suzuki 2010, 2016	0 to 45	80	66.15(5)	141(3)	5.4(2)
This study, Suzuki 2010, 2016	0 to 45	80	65.88(4)	163(1)	4 (fixed)
This study, Suzuki 2010, 2016 (*P2$_1$nm*)	0 to 16	29	66.14(4)	146(2)	4 (fixed)
This study (*Pnnm*)	18 to 45	50	65.3(1)	176(3)	4 (fixed)
Gleason *et al*. 2008	8 to 17	9	66.3(5)	158(5)	4 (fixed)
Suzuki 2010	0 to 9	8	66.20(3)	126(3)	10(1)
Suzuki 2016	0 to 11	13	66.278(6)	135(3)	6.1(9)

Figure 1. Low and moderate pressure structures of ε-FeOOH including the (**a**) *P*2$_1$*nm* structure with ordered hydrogen occupation and asymmetric hydrogen bonds, (**b**) *Pnnm* structure with disordered hydrogen (hydrogen positions are 50% occupied), and (**c**) *Pnnm* structure with symmetric hydrogen bonds. Dashed lines indicate unit cells, oxygen atoms are red spheres, hydrogen atoms are grey spheres, and FeO_6 units are tan polyhedra, which are stacked in edge-sharing chains parallel to the *c*-axis. Image generated in VESTA [Momma and Izumi, 2008]

Figure 2. (a) Unit cell volume, (b) lattice parameters, (c) *a*/*b* and (d) *b*/*c* lattice parameter ratios of FeOOH as a function of pressure, including this study (solid symbols), Suzuki 2010 (black crosses), Suzuki 2016 (black X's), Gleason *et al*., 2008 (open diamonds), Gleason *et al*. 2013 (open triangles), and Ikeda *et al*. 2019 (open circles). Different solid symbols (circles, diamonds, squares) are used to show replicate samples in this study. Green, purple, and yellow symbols indicate that Braggs peaks have been indexed to the $P2_1nm$ (green), high-spin *Pnnm* (purple), and low-spin *Pnnm* (yellow) structures. Light green and light purple lines in (a) represent the equations of state using the parameters from lines 3 and 4 of Table 1, respectively. Error bars reflect uncertainties in the lattice parameters from this study, and when not visible reflect that errors are smaller than the symbols.

Figure 3. Integrated X-ray diffraction patterns of FeOOH at five increasing pressure steps from bottom to top: 44.3 GPa (red), 44.6 GPa, 45.0 GPa, 45.9 GPa, and 46.6 GPa (black), illustrating the structural transition in this pressure interval. Miller indices of ε-FeOOH are shown in red for the lower-pressure *Pnnm* structure, and in black for the higher-pressure, presumably low-spin, structure that is approximately 10% smaller. The Miller indices for the pressure medium (Ne) and gasket material (Re) are shown in grey.

Figure 4. Ambient pressure infrared spectra of $P2_1nm$ ε-FeOOH in the (a) lattice and OH-bending vibrations region and (b) OH-stretching region.

Figure 5. Evolution of the O-H bending frequencies of FeOOH as a function of pressure. The pressure of the $P2_1nm \rightarrow Pnnm$ transition is indicated by a black dashed line. Different colors are used to distinguish the five replicate samples from this study using either Ne as a pressure medium (red, orange) or KBr as a pressure medium (green, blue, purple).

Figure 6. Optical absorption data, including (a) representative optical transmission spectra, indicating the pressure dependent increase in the absorption of ε-FeOOH, and (b) data from five samples of ε-FeOOH, each indicated with a different symbol (diamonds, squares, circles, triangles, and horizontal dashes), showing the change in the ratio of transmitted light (*I*) to

641 incident light (I_0) as a function of pressure (X-axis) and the wavelength of the incident light,
642 which is indicated by color.
643
644 **Supplemental Information**
645
646 **Table S1.** Lattice parameters and unit cell volumes of ε-FeOOH based on X-ray diffraction
647 measurements. Values in parentheses reflect uncertainties. (ATTACHED CSV FILE)
648
649 **Figure S1.** Residuals from the third-order Birch-Murnaghan equation of state fit to ε-FeOOH
650 volume-pressure data from 0 to 45 GPa (Table 1, line 1). Closed black symbols show data
651 collected during compression and open symbols show data collected during decompression.
652
653 **Figure S2.** Eulerian strain (f) versus the normalized pressure (F) of ε-FeOOH, using a V_0 of
654 65.87 $Å^3$ (Table 1, line 1). Closed black symbols show data collected during compression and
655 open symbols show data collected during decompression.
656
657 **Figure S3.** Stacked high-pressure IR spectra of ε-FeOOH including (a) lattice and OH-bending
658 vibrations region and (b) OH-stretching region. Spectra are color coded according to pressure,
659 which are indicated (in GPa) in the legend.
660
661 **Figure S4.** The % maximum FTIR signal intensity collected through the FeOOH sample as a
662 function of pressure. Filled and open symbols are use to indicate duplicate samples used in this
663 study. Dashed red line indicates the predicted pressure of the HS → LS transition from Gleason
664 *et al*. 2013.
665

Figure 1

a) $P2_1nm$, ordered hydrogen

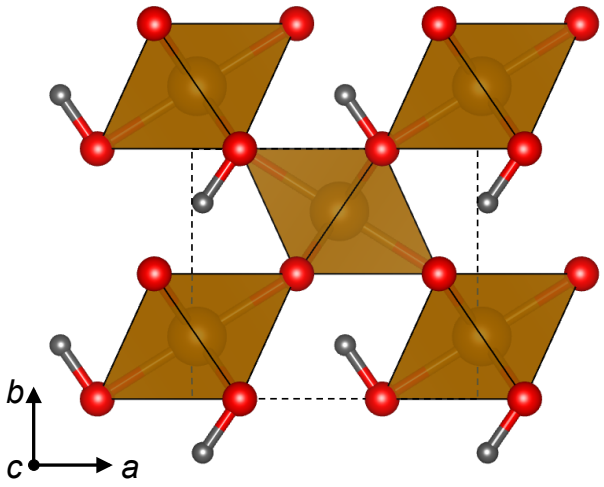

b) *Pnnm*, disordered hydrogen

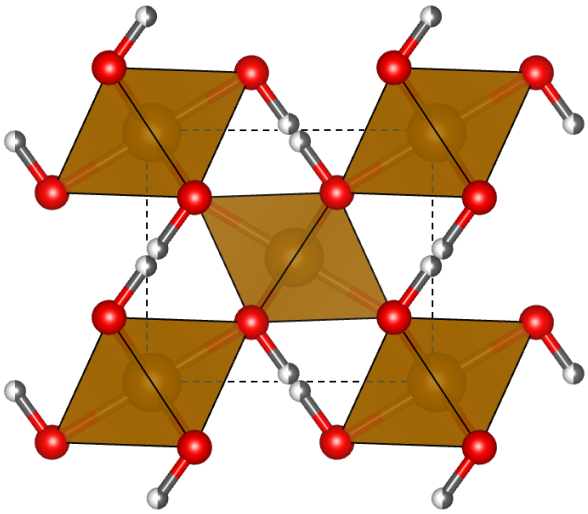

c) *Pnnm*, symmetric hydrogen

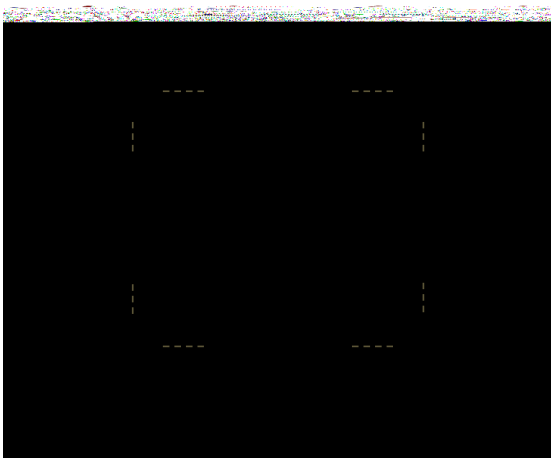

Figure 2

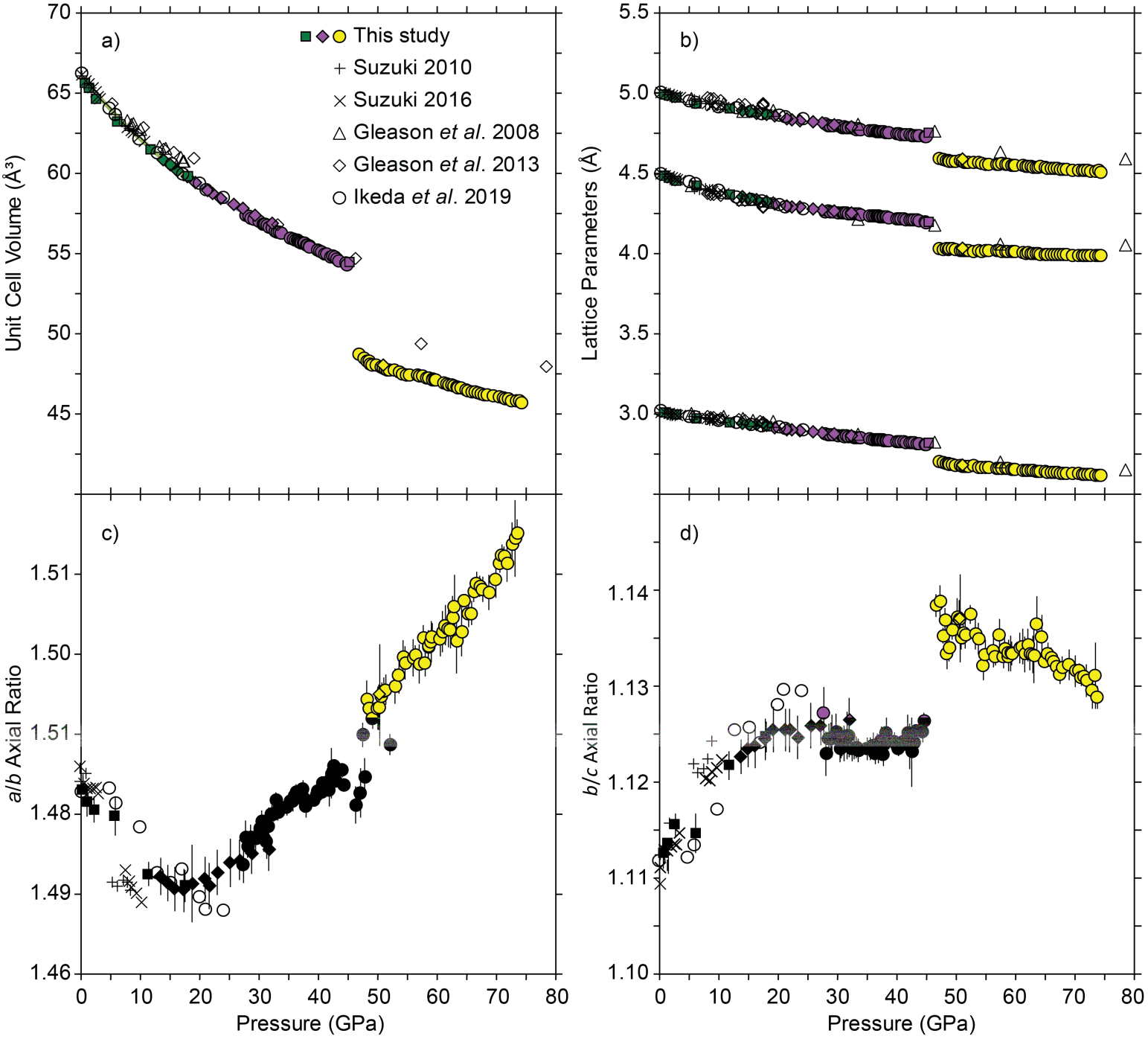
a)
This study
Suzuki 2010
Suzuki 2016
Gleason et al. 2008
Gleason et al. 2013
Ikeda et al. 2019
Unit Cell Volume (Å³)
b)
Lattice Parameters (Å)
c)
a/b Axial Ratio
d)
b/c Axial Ratio
Pressure (GPa)
Pressure (GPa)

Figure 3

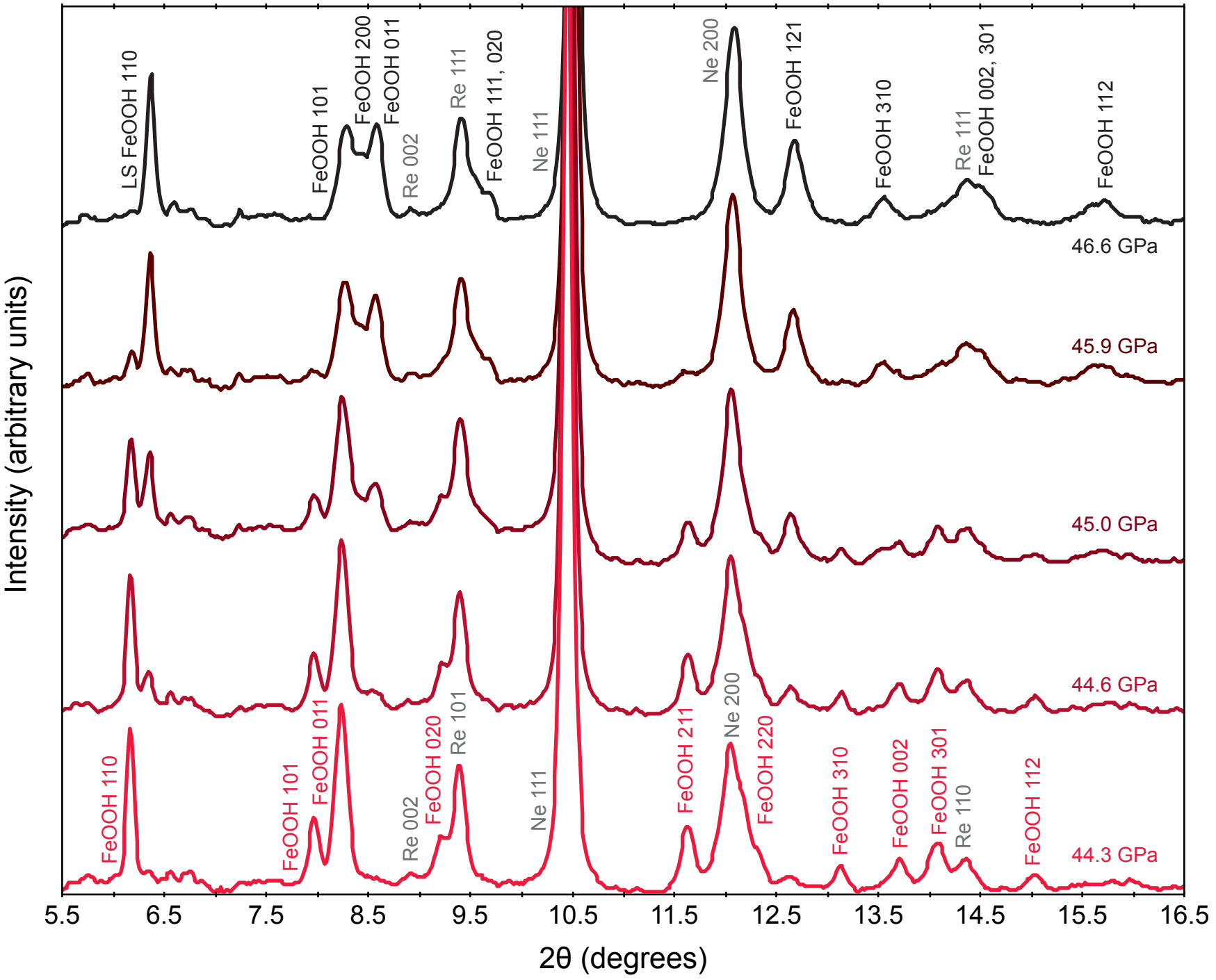
LS FeOOH 110
FeOOH 101
FeOOH 200
FeOOH 011
Re 002
Re 111
FeOOH 111, 020
Ne 111
Ne 200
FeOOH 121
FeOOH 310
Re 111
FeOOH 002, 301
FeOOH 112
46.6 GPa
45.9 GPa
45.0 GPa
44.6 GPa
44.3 GPa
FeOOH 110
FeOOH 101
FeOOH 011
Re 002
FeOOH 020
Re 101
Ne 111
FeOOH 211
Ne 200
FeOOH 220
FeOOH 310
FeOOH 002
FeOOH 301
Re 110
FeOOH 112
Intensity (arbitrary units)
5.5
6.5
7.5
8.5
9.5
10.5
11.5
12.5
13.5
14.5
15.5
16.5
2θ (degrees)

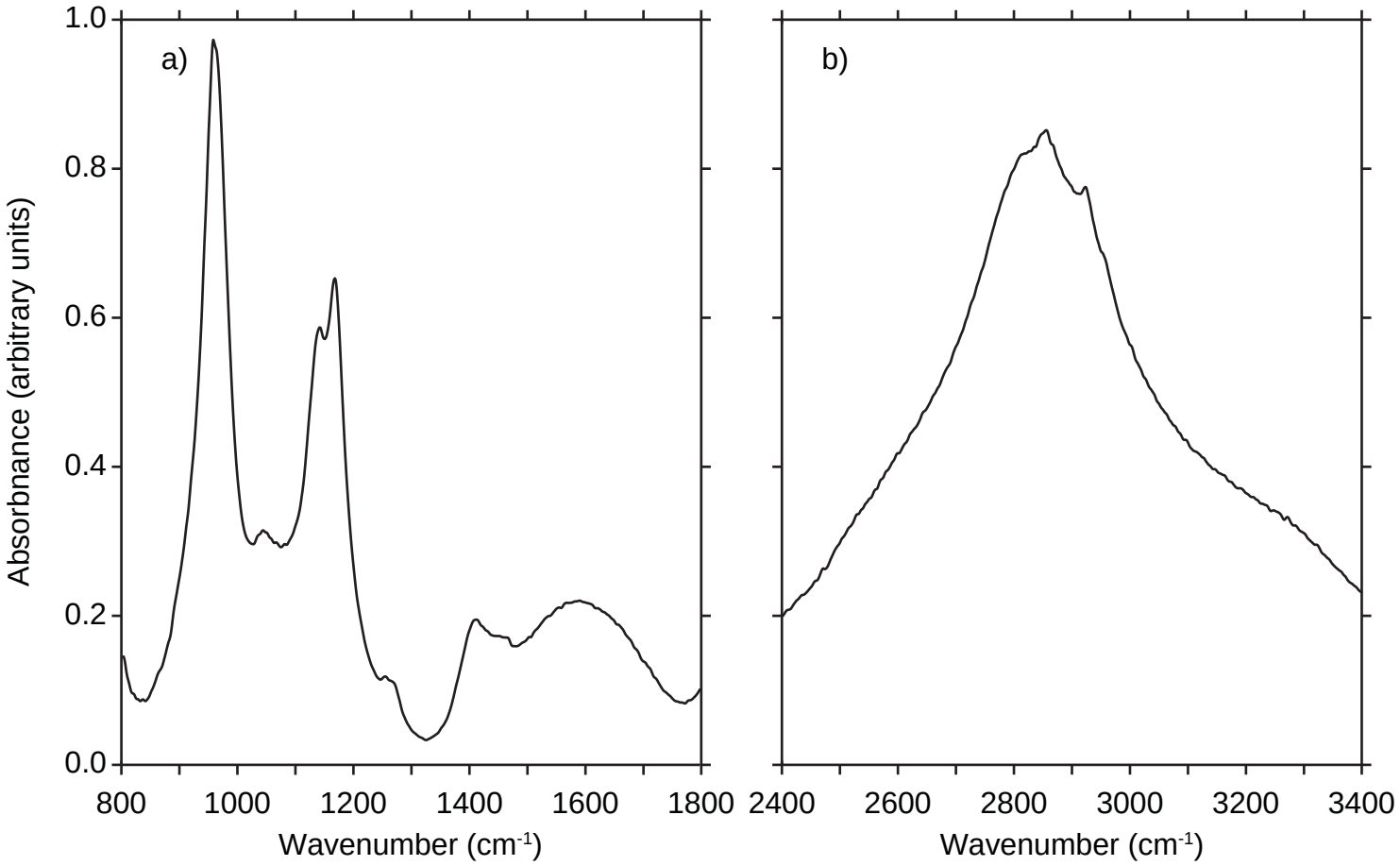
a)
b)
Absorbnance (arbitrary units)
1.0
0.8
0.6
0.4
0.2
0.0
800
1000
1200
1400
1600
1800
2400
2600
2800
3000
3200
3400
Wavenumber (cm-1)
Wavenumber (cm-1)

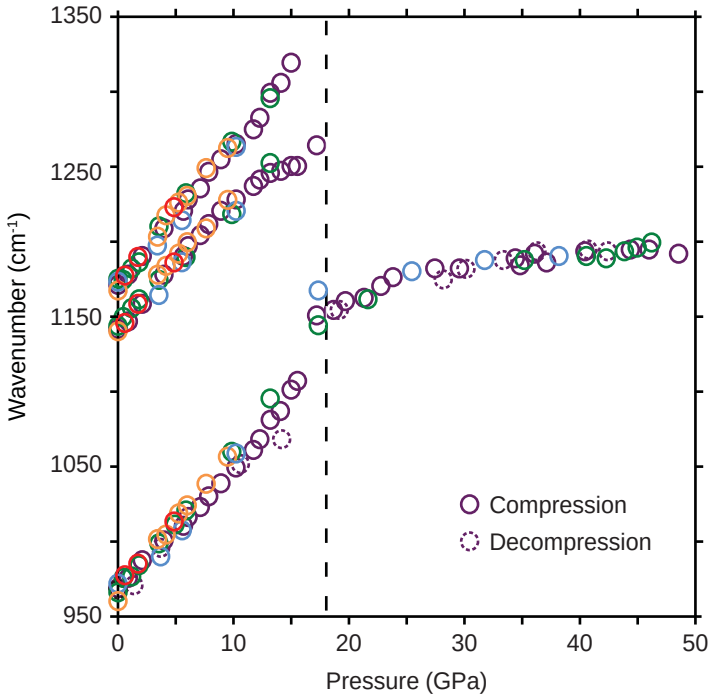
1350
1250
1150
1050
950
Wavenumber (cm-1)
0
10
20
30
40
50
Pressure (GPa)
Compression
Decompression

Figure 6

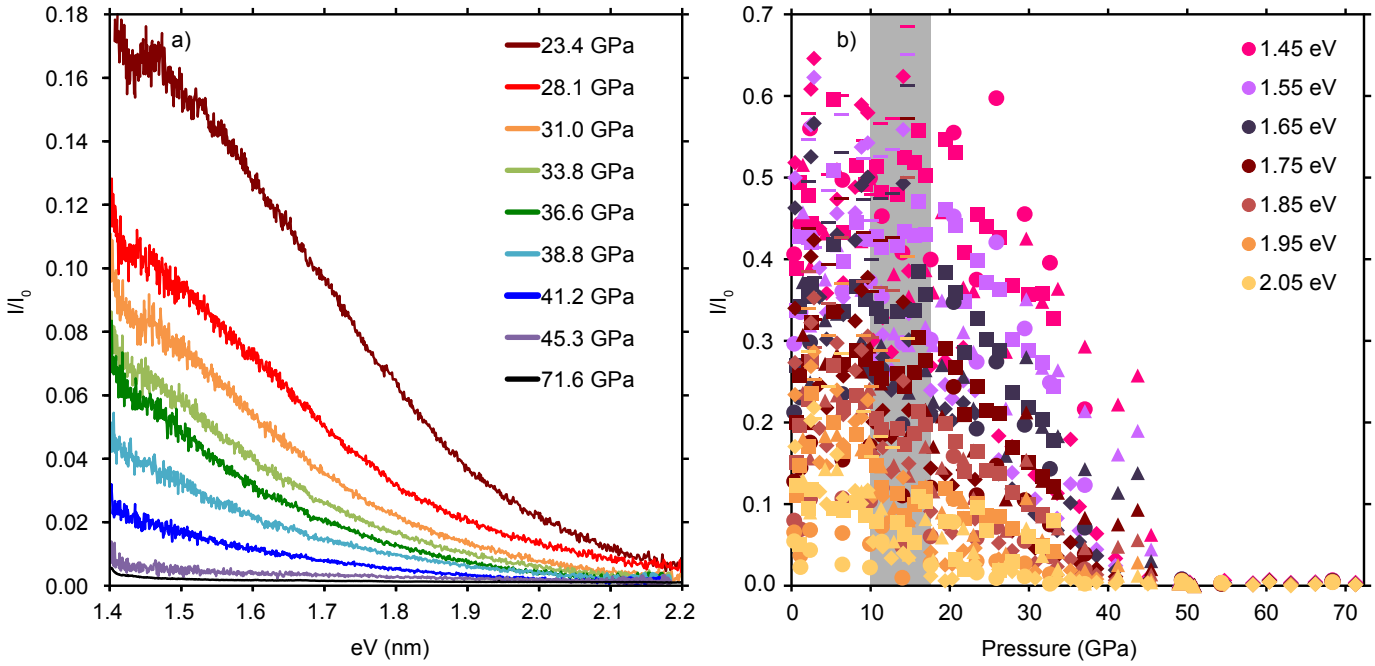
a)
23.4 GPa
28.1 GPa
31.0 GPa
33.8 GPa
36.6 GPa
38.8 GPa
41.2 GPa
45.3 GPa
71.6 GPa
I/I0
eV (nm)
b)
1.45 eV
1.55 eV
1.65 eV
1.75 eV
1.85 eV
1.95 eV
2.05 eV
I/I0
Pressure (GPa)